

Sub-km scale numerical weather prediction **model simulations** of radiation fog

Daniel K.E. Smith¹ | Ian A. Renfrew¹ | Stephen R. Dorling¹ | Jeremy D. Price² | Ian A. Boutle²

¹School of Environmental Sciences,
University of East Anglia, Norwich, Norfolk,
NR4 7TJ, UK

²Met Office, Exeter, UK

Correspondence

Daniel K.E. Smith, School of Environmental
Sciences, University of East Anglia,
Norwich, Norfolk, NR4 7TJ, UK
Email: d.smith5@uea.ac.uk

Funding information

NERC Grant NE/M010325/1

The numerical weather prediction (NWP) of fog remains a challenge with accurate forecasts relying on the representation of many interacting physical processes. The recent local and non-local fog experiment (LANFEX) has generated a detailed observational dataset creating a unique opportunity to assess the NWP of fog events. We evaluate the performance of **operational and research configurations** of the Met Office Unified Model (MetUM) with three horizontal **grid-lengths**, 1.5 km, 333 m and 100 m, in simulating four LANFEX case studies. In general, the sub-km scale versions of the MetUM are in better agreement with the observations, however there are a number of systematic model deficiencies. The MetUM produces valleys that are too warm and hills that are too cold, leading to valleys that do not have enough fog and hills that have too much. A large sensitivity to soil temperature was identified from a set of parametrisation sensitivity experiments. In all the case studies, the model erroneously transfers heat too readily through the soil to the surface preventing fog formation. Sensitivity tests show that the specification of **the soil thermal conductivity parametrisation** can lead to up to a 5-hour change in fog onset time. Overall the sub-km models demonstrate promise but they have a high sensitivity to surface properties.

KEYWORDS

Radiation fog, NWP, Boundary-Layer, Soil thermal conductivity

1 | INTRODUCTION

Fog has large human and environmental impacts which are often understated; the reduction in visibility caused by fog leads to huge disruptions for air, sea and land transport. The financial and human losses are comparable to losses from tornadoes or severe tropical storms (Gultepe et al., 2007). Fog is the second most likely cause of weather related aviation accidents behind strong winds (Gultepe et al., 2019). Over 10,000 people died in India in 2017 from fog related traffic accidents (Kapoor, 2019). Similarly in the US, between 1995 and 2004, 13,720 people were reported to have died in fog related accidents (Forthun et al., 2006). Fog and low cloud can have a destabilising effect on electricity grids due to the rapid change in radiation conditions for photo-voltaic installations (Köhler et al., 2017). Fog can also lead to persistent temperature inversions which result in pollution stagnating in the lower atmosphere for extended periods with consequences for human health (Tanaka et al., 1998, Nemery et al., 2001). An example of the impact fog can have was the widespread fog event of the 2nd November 2015 which resulted in the cancellation of flights from airports across the UK, in particular Heathrow airport where over 112 flights were cancelled (Cleaton, 2015). Other methods of transport were also disrupted with speed restrictions implemented on roads, reports of traffic accidents due to the fog and the cancellation of ferries.

In contrast, fog can also have a positive impact on human life. In arid regions, fog water can be collected as an additional fresh water source (Schemenauer et al., 1988), while in the Montane cloud forests of Taiwan, fog is a regulator for the entire ecosystem (Li et al., 2015). In California's central valley, daytime fog enhances the winter chill essential for improving crop yield in the following season's buds, flowers and fruits (Baldocchi and Waller, 2014).

Radiation fog forms primarily by radiative cooling, under clear skies, within a nocturnal surface inversion and with low levels of turbulence leading to near-surface saturation (Price, 2019). It develops **vertically** within the stable boundary-layer and is referred to as shallow stable radiation fog hereafter. As the fog deepens, it can become **opaque** to longwave radiation (in the 8–12 μm range **commonly measured by instrumentation**), and therefore defined as **optically thick fog**. An **optically thick fog** cools from the fog top generating turbulence from the weak convection created as the negatively buoyant air at the fog top sinks. After on average two hours, this causes a transition in boundary-layer stability from stable to well-mixed (Price, 2011). Within this well-mixed boundary-layer a deep adiabatic radiation fog can develop i.e. the lapse rate becomes saturated adiabatic. This boundary-layer stability transition occurs in around 50% of radiation fog cases **seen at the Met Office Meteorological Research Unit based at Cardington, Bedfordshire, UK** (Price, 2011). Deep adiabatic radiation fogs are typically longer lived with a greater potential to persist during the day and thus with a greater impact (Price, 2011). The stability transition is sensitive to various conditions including aerosol concentrations (Boutle et al., 2018; Poku et al., 2019), wind speed and humidity (Smith et al., 2018).

To mitigate against the socio-economic impacts of fog a reliable forecast is essential. Accurately simulating fog in numerical weather prediction (NWP) models remains a huge challenge due to the complex feedbacks between key processes including radiative cooling, turbulence, microphysics and surface interactions (e.g. Tudor, 2010; Van der Velde et al., 2010; Steeneveld et al., 2014; **Pu et al., 2016**). Fog is influenced by many factors that NWP models cannot fully resolve. Unfortunately many of these processes interact with each other and are highly sensitive, often leading to unreliable and overly sensitive model configurations. Compensating errors in parametrised processes are common place (Steeneveld and de Bode, 2018).

Sub-km scale models are becoming a realistic possibility for fog forecasting due to increasing computational re-

39 sources. At present they are often restricted to relatively small areas where the population density is large and the
40 impact of fog is greatest, i.e. city-scale models. The high horizontal resolution of these models allows them to partially
41 resolve surface and topographic heterogeneities and consequently processes that impact the spatial variability of fog
42 (Vosper et al., 2013) including advection and turbulence caused by drainage flows and cold pool formation (Porson
43 et al., 2011; Hang et al., 2016; Gultepe et al., 2016; Price, 2019; Ducongé et al., 2020). One of the earliest examples is
44 the London Model (Boutle et al., 2016) which has been running semi-operationally since September 2013 with other
45 versions being developed for additional locations (e.g. Delhi - Jayakumar et al., 2018).

46 Correctly representing the interaction between the atmosphere and the surface can be key to modelling the
47 formation and development of fog (Steenefeld and de Bode, 2018). Land surface properties such as the land use
48 dataset (Jayakumar et al., 2018), thermal roughness (Weston et al., 2019), albedo, snow depth (Zhang and Pu, 2019)
49 and soil properties (Duykerke, 1999; Guedalia and Bergot, 1994; Bergot and Guedalia, 1994; Maronga and Bosveld,
50 2017; Steeneveld and de Bode, 2018) in addition to the land surface model (Chachere and Pu, 2019; Weston et al.,
51 2019) are all critical. One key soil property investigated in 1D models is the soil thermal conductivity (Bergot and
52 Guedalia, 1994; Steeneveld and de Bode, 2018). Both Bergot and Guedalia (1994) and Steeneveld and de Bode (2018)
53 found that fog onset was sensitive to the specification of the soil thermal conductivity. Indeed, the latter found the soil
54 thermal conductivity and turbulent boundary-layer mixing the most influential parameters affecting fog onset. These
55 studies show the impact that the surface component of models have on simulations of fog but many of these use 1D
56 models without advective processes. It is also necessary to understand how sensitive the recently developed sub-km
57 scale models are to aspects of the surface model such as the soil thermal conductivity. Additionally, heterogeneities
58 in the soil may feedback on the near surface dynamics and thus quantifying model sensitivities is crucial. The removal
59 of moisture at the surface via processes such as dew deposition (Bergot et al., 2007), gravitational settling of droplets
60 (Müller et al., 2010) and the direct impact of droplets on vegetation (Von Glasow and Bott, 1999) are crucial for
61 the accurate prediction of fog events.

62 We use four cases from the Local and Non-Local Fog experiment (LANFEX), a recent field campaign undertaken
63 in the UK, to improve the understanding and modelling of fog events (Price et al., 2018). Understanding the sensitivity
64 of sub-km NWP models to different processes is crucial for their development. LANSFEX provides a bespoke set of
65 high spatial resolution observations in two locations ideal for a detailed evaluation. Previous evaluations have been
66 limited by a single site or lower spatial resolution observations. Using the LANSFEX observations and the Met Office
67 Unified model (MetUM) we evaluate the performance of three configurations of the MetUM with different horizontal
68 grid-lengths in simulating radiation fog events. Specifically, we evaluate the performance of the current operational
69 version for the UK (Bush et al., 2019), a sub-km scale NWP configuration similar to the London Model (Boutle et al.,
70 2016) and a research version with 100 m grid-length similar to Vosper et al. (2013). We will also assess the sensitivity
71 of the simulated fog to the soil thermal conductivity parametrisation in a sub-km scale configuration.

72 | 2 | MODEL, OBSERVATIONAL AND CASE STUDY DETAILS

73 | 2.1 | Observations

74 We utilise data collected during the LANSFEX field campaign (Price et al., 2018). LANSFEX ran from November 2014 until
75 April 2016 and was organised by the UK Met Office Meteorological Research Unit based at Cardington, Bedfordshire.
76 The experiment was designed to investigate the life-cycle of radiation fog in two areas of contrasting orography: one
77 in Bedfordshire which is relatively flat (Figure 1) and one in Shropshire which has more complex orography (Figure 2).
78 Over the study period continuous measurements were taken at various locations with additional measurements taken

79 during intensive observation periods (IOPs) via a tethered balloon, radiosondes and an infrared camera (see Price et al.
80 (2018) for details).

81 Cardington, Bedfordshire (52°06'N 0°25.5' W) is located in a wide shallow valley surrounded by arable fields with
82 low hedges. The valley is approximately 10 km wide at Cardington, rises at its sides by 30 - 40 m and has a down-valley
83 gradient of 1:375 or 0.15° (Figure 1). The relatively homogeneous orography of the Cardington area allows the study
84 of fogs where advective effects are believed to be relatively small, although they can still have an impact (Porson et al.,
85 2011).

86 The Shropshire region (centred on 52°25.2'N, 3°6' W) was chosen for its array of moderate hills and valleys (Figure
87 2). These range in width from 1-4 km and in valley to hilltop height from 100-150 m. Land use is mostly pasture with
88 low hedges and some forestry. The Shropshire system of valleys provide conditions where both in-situ and advective
89 processes, such as the formation of cold pools and katabatic or anabatic flows, play an important role in all stages of
90 a fog event.

91 Two types of observing stations were deployed: in total, 13 smaller fog-monitor stations and 6 more extensively
92 instrumented main sites. The fog monitor sites were single weather stations which measured screen temperature and
93 relative humidity, 2.5 m winds, surface pressure and a prototype fog droplet spectrometer designed to capture the
94 microphysical properties of fog. The main sites had a variety of in-situ and remote sensing equipment, such as Lidars,
95 each site with a slightly different suite of instruments. These sites were based around a mast (10, 16 or 50 m) which
96 was extensively instrumented. A breakdown of the instrumentation and the uncertainty in the measurements can be
97 found in Price et al. (2018).

98 2.2 | Selected Case Studies

99 We chose four out of the nineteen IOPs from LANFEX as case studies: IOPs, 1, 12, 17 and 18. IOPs 1, 17 and 18 were
100 at the Bedfordshire location and IOP12 at the Shropshire location. The four cases were selected to be representative
101 of a variety of foggy events and have high data availability. These four case studies were chosen to be distinct with a
102 broad range of conditions and evolutions, as briefly described here:

- 103 • *IOP1 - 24th/25th Nov 2014 - Cardington.* A case of prolonged shallow stable radiation fog which persisted for
104 10 hours then transitioned to a deep adiabatic radiation fog for an hour before dissipation. This case was se-
105 lected to test the model's performance for fog in a stable boundary-layer with clear skies. This case study was
106 the focus of Boutle et al. (2018) who used the LANFEX data, the operational Met Office Unified Model and the
107 UCLALES-SALSA LES model to investigate aerosol-fog interactions. Here, we complement this work by investi-
108 gating the impact of horizontal resolution and surface interaction on fog representation.
- 109 • *IOP12 - 1st/2nd Oct 2015 - Shropshire.* A case of thin spatially varying fog followed by a cloudy interlude and then
110 a period of deeper fog constrained to the valleys. Limited observations from IOP12 were presented in Price et al.
111 (2018) to illustrate the heterogeneity of fog in a complex valley system and to briefly assess the performance
112 of two different NWP models (the MetUM and Meso-NH) at 100 m horizontal resolution. **The Meso-NH model
113 at 100 m horizontal resolution is analysed in detail by Ducongé et al. (2020).** Here, we expand this analysis to
114 evaluate the MetUM with grid-lengths of 1.5 km, 333 m and 100 m as well as parametrisation sensitivity.
- 115 • *IOP17 - 20th/21st Jan 2016 - Cardington.* A case of patchy fog for a short period during the night which did
116 not develop into a persistent fog. This case enables the assessment of the model for a fog case with variable
117 and relatively strong wind speeds, which were observed to be key to the patchy nature of the fog and its short
118 duration.

- 119 • *IOP18 - 10th/11th Mar 2016 - Cardington*. A shallow stable radiation fog case with a rapid transition into a deep
120 adiabatic radiation fog. This case will be used to assess the model's performance in simulating fog within a well-
121 mixed boundary-layer.

122 2.3 | The Met Office Unified Model

123 The MetUM solves the non-hydrostatic, deep atmosphere equations of motion using a semi-implicit, semi-Lagrangian
124 numerical scheme (Wood et al., 2014). The model is run on a Arakawa C staggered grid (Arakawa and Lamb, 1977) with
125 rotated latitude/longitude coordinates and a Charney-Phillips staggered hybrid-height terrain-following coordinate
126 system in the vertical (Charney and Phillips, 1953). The main prognostic variables are potential temperature, pressure,
127 density, five moisture variables (vapour, liquid, rain, ice and graupel) and the three components of wind. **The MetUM**
128 **contains a set of physical parametrisations to represent the effect of sub-grid scale processes. The MetUM is designed**
129 **to be somewhat "scale aware" and as such some parametrisations have been designed so it is not necessary to change**
130 **them manually when altering the resolution (e.g. boundary-layer scheme - Boutle et al., 2014b and microphysics**
131 **scheme - Boutle et al., 2014a). MetUM parametrisations include radiation (based on Edwards and Slingo, 1996), a**
132 **blended boundary-layer scheme for turbulent mixing (Boutle et al., 2014b), a sub-grid cloud parametrisation (based on**
133 **Smith, 1990) and a mixed-phase cloud microphysics parametrisation (based on Wilson and Ballard, 1999 with various**
134 **adjustments for example Boutle et al., 2014a and Boutle et al., 2018). The blended boundary-layer scheme (Boutle**
135 **et al., 2014b) is used that blends the 1D scheme of Lock et al. (2000) with the 3D Smagorinsky scheme, dependent**
136 **on the resolution and flow regime, allowing for a seamless transition at higher resolutions. In stable boundary-layers**
137 **the 1D scheme uses the "Sharpest" stability function (Lock et al., 2000).**

138 The MetUM is coupled to the Joint UK Land Environment simulator (JULES) (Best et al., 2011). JULES contains
139 information about the properties of the land surface such as albedo and surface roughness. It models the soil moisture
140 and temperature providing the surface boundary conditions to the MetUM. The soil model has 4 vertical levels and
141 calculates the fluxes of temperature and moisture between the vertical levels. JULES uses a tile scheme approach,
142 with each grid-point containing a fraction of 9 different land surface tiles each with their own roughness length and
143 albedo as well as other properties; 5 for vegetation and 4 for non-vegetation.

144 The MetUM has a broad range of uses across multiple scales from global (Walters et al., 2019) to regional (Bush
145 et al., 2019) to city scale (Boutle et al., 2016). At regional scales there are two configurations; for the mid-latitudes
146 and for the tropics (Bush et al., 2019). We use the mid-latitude configuration.

147 Certain parametrisations are particularly relevant for radiation fog. Droplet settling, for example, is the process of
148 cloud droplets falling under gravity and it is calculated using Stoke's law. Another aspect of the microphysics scheme
149 which directly impacts fog liquid water content is the prescribed reduction in the number of droplets near the surface;
150 this "droplet taper" was introduced into the MetUM by Wilkinson et al. (2013) and has recently been developed
151 further (Boutle et al., 2018). Current operational versions of the MetUM use a fixed droplet number of 50 cm^{-1} from
152 the surface up to 50 m and then taper to an aerosol dependent value at 150 m altitude. **Other LANFEX studies have**
153 **focussed on fog microphysics (Boutle et al., 2018; Poku et al., 2019; Ducongé et al., 2020). The microphysics scheme**
154 **used here was evaluated for fog against the LANFEX observations and large-eddy simulations (Boutle et al., 2018).**
155 **The reduced droplet number offered a statistical improvement in an evaluation against an independent data set.**

156 The MetUM contains a prognostic single-species aerosol which is used to calculate visibility and droplet number
157 above the fixed droplet taper height threshold, 150 m. The current visibility diagnostic (Clark et al., 2008) uses a single
158 monodisperse dry aerosol concentration which is hydrated, based on screen temperature and humidity, using a Köhler
159 curve. Given sufficient moisture, the scheme forms fog with the size and the number of particles used to calculate

160 the extinction coefficient which is used (in a version of Koschmieder's Law) to calculate visibility such that

$$161 \quad \text{Visibility} = \frac{-\ln(\epsilon)}{Nr_m^2\beta_0 + \beta_{air}} \quad (1)$$

162 where ϵ is the liminal contrast given a value of 0.02, N is aerosol number density, r_m is mean droplet radius, β_0 is a
163 constant to account for the complexities of size spectra and scattering and β_{air} is the extinction coefficient of clean
air. The scheme's aerosol is a single size and has a fixed hygroscopy value resulting in single sized droplets.

164 We run the MetUM with three grid-lengths, 1.5 km, 333 m and 100 m, for the selected LANFEX case studies,
165 referred to as UM1.5, UM333 and UM100 respectively. The UM1.5 is currently the operational configuration and
166 resolution of the MetUM for the UK (Bush et al., 2019), the UM333 is similar to the London Model (Boutle et al.,
167 2016) but with the domain moved to the LANFEX sites and the UM100 is similar to the version discussed by Vosper
168 et al. (2013), Vosper et al. (2014) and Price et al. (2018). All simulations are initialised at 1200 UTC to capture the
169 pre-fog cooling period. An examination of a 1500 UTC initialisation for IOP1 found the MetUM was unable to cool
170 sufficiently and had a warm bias of 2 K by 1600 UTC. This result is similar to that shown recently using other NWP
171 models such as Román-Cascón et al. (2016), Lin et al. (2017) and Chachere and Pu (2019). For example, Lin et al.
172 (2017) found there was a trade-off between using a shorter lead time, which has more accurate initial conditions, and
173 using a longer lead time, which has less accurate initial conditions but longer spin-up time. Considering the results of
174 Lin et al. (2017) and the results from the IOP1 simulations, an initialisation time of 1200 UTC is a good compromise
175 between ensuring accurate initial conditions and sufficient spin-up of the pre-fog cooling period.

176 There are other differences between the three configurations with different grid-lengths (Table 1). As the grid-
177 length decreases it is also necessary to reduce the time step to ensure numerical stability. The UM100 is run with 140
178 vertical levels as Vosper et al. (2013) showed that increasing the vertical resolution improved the simulations of cold
179 pools. The other key difference between simulations is the critical relative humidity (RHCrit) parameter, the grid-box
180 mean relative humidity at which condensation begins to occur in a grid-box. This parameter is designed to allow for
181 the sub-grid scale variability of relative humidity and thus partial cloudiness within a grid-box. At higher resolutions
182 some of the sub-grid humidity variability is resolved and thus a higher RHCrit is appropriate.

183 The UM1.5 is initialised from its own analysis with a full 3D VAR data assimilation and forced at its lateral boundary
184 by the global version of the MetUM (Walters et al., 2017). The UM100 and UM333 are initialised from the UM1.5
185 analysis, including sub-surface parameters, and are one-way nested within the UM1.5 with the boundary conditions
186 updated every 15 minutes. The initialisation and nesting configuration are identical to those used in the London Model
187 (Boutle et al., 2016). In the Bedfordshire domain (Figure 1) the main valley is resolved by UM1.5 with the other two
188 resolutions producing a lot more detail in the tributary valleys. The orography in the Shropshire domain (Figure 2) is
189 more complex, with UM1.5 only resolving the widest most easterly valley. Both the UM100 and UM333 orography
190 resolve greater detail; UM333 captures the main valleys and ridges, but the detail in the narrowest valleys and ridges
191 is lost.

192 The specification of land use is at the same resolution as the grid-length of the atmospheric model. The land use
193 dataset uses the Institute of Terrestrial Ecology (now part of the Centre for Ecology and Hydrology) dataset (Bunce
194 et al., 1990) which has a resolution of 25 m and is re-configured to the model grid. Both domains are located in
195 generally rural areas and are dominated by the mid-latitude grass surface type. Boutle et al. (2016) performed a
196 sensitivity test using the UM333 with the UM1.5 orography and found the fog in their simulation was spatially similar
197 to the control UM1.5 simulation i.e. the orography resolutions dominated the simulations of fog.

198 3 | RESULTS

199 3.1 | Horizontal Resolution Investigation

200 Here we discuss the performance of the UM1.5, UM333 and UM100 for the selected LANFEX case studies. In general,
201 the MetUM produces valleys that are too warm after 1800 UTC and hills that are too cold after 1500 UTC (Figure 3).
202 For the Bedfordshire simulations, the valley nocturnal warm bias improves with resolution. The UM1.5 has a valley
203 warm bias of 2 K at 0000 UTC compared to a 1 K bias for the UM333 and a 0.5 K for the UM100 configuration. The
204 difference in the temperature biases for the hill sites is very small indicating the benefit of the smaller grid-length on
205 pre-fog temperature evolution is within the valleys in the Bedfordshire domain.

206 Using IOP12 to assess the MetUM at the orographically more complex location in Shropshire, the general be-
207 haviour is similar to the Bedfordshire area with the valleys too warm and hills too cold after 1800 UTC. The UM1.5 is
208 too cold overnight on the hills by more than 2 K by 0000 UTC, and too warm in the valleys by around 1.5 K, as it is not
209 resolving the orographically driven flows in the Shropshire area. The UM333 represents the near-surface temperature
210 closest to the observations with a valley warm bias of around 1 K at 0000 UTC and hill cold bias of 0.5 K. Surprisingly,
211 the UM100 is warmer than the UM333 in the valleys, with an average bias of 3 K by 0000 UTC and a trend which is
212 very similar to the UM1.5 configuration. The UM100 on the hills also has a cold bias and is particularly cold between
213 2000 UTC and 2200 UTC with a bias of approximately -2.5 K.

214 To investigate the relatively poor performance of the UM100 for temperature we performed sensitivity tests by
215 reducing the domain size of the UM333 to the same size as the UM100 (Table 1). The smaller domain resulted in a
216 similar bias, up to 3 K in the valleys, to that seen in the UM100 and UM1.5. The influence of the boundary conditions
217 was clear throughout the entire domain. This implies that the UM100 is run over a domain which is heavily influenced
218 by the boundary conditions even over relatively short periods of time. Part of the benefit of using the UM100 is to
219 improve the near-surface cooling through a better representation of the surface but this potential improvement is
220 partially negated by advection from the boundaries. Lean et al. (2019) also ran the MetUM with 100 m grid length
221 for a domain size of 80 km x 80 km and 30 km x 30 km, similar to the two domain sizes used in our sensitivity
222 experiments. They found it was necessary to use a larger domain to avoid spin-up effects penetrating into the area
223 of interest in clear sky convective boundary-layer situations. We find that the domain size also has an influence on
224 screen temperature even in low-wind situations, so this will be a contributing factor to the bias seen in the LANFEX
225 cases using 100 m grid-length.

226 The spatial features of the temperature evolution simulated by the three configurations during the early night
227 of IOP12 can be compared (Figure 4). At 1800 UTC all three configurations have a similar temperature pattern with
228 warmer air to the east. By 2100 UTC the difference between simulations is pronounced. UM333 is coldest across
229 the whole domain. The UM1.5 does not resolve the spatial variability in temperature, not capturing the hill-valley
230 temperature difference observed. Despite the larger bias in the UM100 simulation the contrast between the hill and
231 valley temperatures is more apparent than in the other simulations, but these do not verify as well as the UM333
232 when compared to the point observations (Figure 3b). This is partly because the UM333 simulation is generally colder
233 which better matches the observations.

234 In short, all three configurations of the MetUM evolve valleys that are too warm and hills that are too cold for these
235 radiation fog cases. This is also evident for each Bedfordshire IOP separately, as well as averaged together (Figure
236 3a). The sub-km scale simulations outperform the UM1.5 in terms of the nocturnal cooling within the valleys in both
237 locations, except the UM100 at Shropshire which is very similar to the UM1.5. On the hills the temperature evolution
238 is very similar between all three configurations with the UM333 slightly outperforming the other two configurations

239 and comparing well with the observed temperature in the Shropshire area. Our results here are contrary to Hughes
240 et al. (2015) who found that a version of the UM100 had a cold bias in the daily minimum temperature, particularly
241 at a valley site, due to a lack of cloud in the UM100. Here, only IOP12 was influenced by cloud and this is discussed
242 further in section 4.

243 The pre-fog temperature biases seen in these four cases are expected to impact the timing of fog formation.
244 All three simulations produce fog for all the events at all the sites, except for IOP17, where the lower resolutions
245 have no fog (Figure 5). In IOP12 fog is simulated for the hilltop site (Springhill) where none was observed. In most
246 comparisons the simulated fog duration is too short. In general, the UM100 forms fog earlier than the other two
247 resolutions, particularly for the Bedfordshire cases, consistent with the pre-fog cooling in the UM100 being closer to
248 the observations (Figure 3). However, UM333 forms fog the latest, which is generally less accurate compared to the
249 observations, despite having a smaller warm bias than UM1.5. The delay in fog onset in the UM333 compared to the
250 UM1.5 appears to be caused by subtle differences in specific humidity, $\sim 0.1 \text{ g kg}^{-1}$ drier in the lowest 100 m in the
251 UM333.

252 Looking at IOP12 and the spatial variation in the time fog forms, UM1.5 is unable to correctly simulate the spatial
253 distribution of fog (Figure 5). For example, the UM1.5 does not produce fog at the Jaybarns site despite the compar-
254 atively prolonged fog observed, while conversely, it over produces fog at the Springhill site. Given the temperature
255 biases in the UM1.5 this is the expected result: the valleys are not foggy enough and the hills are too foggy. The
256 UM100 and UM333 simulate fog onset times more realistically than the UM1.5 (e.g. IOP12 at Jaybarns) but they do
257 also have similar issues: forming too much fog on the hills and delaying formation in the valleys. IOP17 emphasises the
258 benefit of using the UM100 configuration, as this is the only simulation able to reproduce the very shallow transient
259 fog observed during this case study. In IOP18, all of the simulations form fog late, but the UM100 is closest to the
260 observations.

261 Another important aspect of the fog life-cycle is the boundary-layer stability transition, which is illustrated by the
262 change in hatching in figure 5. Following Price (2011), modified to account for different instrument heights, we define
263 this transition as when the screen and 25 m temperatures are within 0.1 K. Where the highest tower observation is
264 lower than 25 m, the temperature from the highest observation and the closest model level are used. Note this gives
265 a discrete time for the stability transition, whereas in reality this processes takes on average 2 hours (Price, 2011). In
266 general, the simulated stability transition is similar to that observed. For IOP1 all three simulations produce shallow
267 stable radiation fog but do not reproduce the short period of deep adiabatic radiation fog. Overall, the UM100 for
268 IOP12 performs better than the other simulations for the stability transition process, particularly at Jaybarns and
269 Pentre. For IOP18 at Cardington the MetUM is unable to reproduce the shallow stable radiation fog period from
270 2200 UTC until 0400 UTC. However, all configurations produce the deep adiabatic radiation fog with the UM100 the
271 only configuration which produces a short period of shallow stable radiation fog. In summary the UM100 appears to
272 have the best fog formation and stability transition timing but the overall accuracy is limited.

273 If the MetUM produces fog, the subsequent timing of dissipation appears relatively insensitive to the configura-
274 tion used - differences in dissipation time between the resolutions is at most 1 hour 15 minutes. The MetUM generally
275 dissipates fog earlier than observed, by typically 1 hour, as is seen at nearly all sites and cases. This result is similar
276 to that found by Price et al. (2015) who found that no members of a MetUM ensemble forecast were able to repro-
277 duce fog that persisted during the day. This early dissipation of fog in the MetUM is a cause for concern, but is not
278 investigated further here and instead is reserved for future studies.

279 The spatial distribution of liquid water content (LWC) is another key difference between the three MetUM simu-
280 lations (Figure 6). For IOP1 the spatial distribution of fog in the UM1.5 simulation is very similar to the UM100 run
281 with a similar area of fog located to the south-west and the centre of the domain. The similarity between the UM1.5

282 and UM100 can partly be attributed to the domain size as mentioned in relation to the near-surface temperature.
283 The sensitivity test using the UM333 with a reduced domain also produces a similar spatial distribution of LWC as the
284 UM1.5 and UM100 for IOP1. In the UM333 simulation the fog to the centre of the domain is not present and the fog
285 area to the south-west covers a smaller area. For IOP12 the fog is generally constrained to the valleys and is much
286 denser in UM100 than UM333. Indeed the UM100 and the UM1.5 generally produce more fog than the UM333
287 which simulates patchier fog.

288 Given the deficiency in the representation of valley cooling it is vital to assess the model representation of valley
289 dynamics to see if these flows lead to excessive mixing in the boundary-layer, which would be preventing cooling
290 near the surface. In general the UM100 does resolve near surface flows better than UM333 and UM1.5 (not shown).
291 Given the good representation of the valley flow in the UM100, and the reasonable representation in UM333, errors
292 in the valley winds are unlikely to be the cause of the valley temperature biases. These results here are similar to
293 those found by Vosper et al. (2013) who showed that the MetUM with 100 m grid-length, a very similar set-up to the
294 UM100 used here, was in good agreement with the observed winds in a valley system and an improvement compared
295 to the operational MetUM with 1.5 km grid-length.

296 In summary, the sub-km versions of the MetUM outperform the UM1.5. However, temperature biases remain;
297 the valleys are too warm and hills are too cold leading to valleys that are not foggy enough and hills that are too foggy.
298 The following section investigates potential causes for these biases through sensitivity experiments that highlight
299 improvement opportunities.

300 3.2 | Soil thermal conductivity investigation

301 The interaction between fog and the underlying surface has a key role in the life-cycle of fog events and so the
302 modelling of fog is sensitive to the land surface model (Chachere and Pu, 2019; Weston et al., 2019). In particular the
303 soil thermal conductivity has been shown to be crucial in accurately simulating fog onset (Bergot and Guedalia, 1994;
304 Steeneveld and de Bode, 2018). Here we assess the ability of the MetUM to realistically simulate the soil heat flux
305 and examine the sensitivity to the soil thermal conductivity parametrisation.

306 The initial soil temperature is simulated very similar to the observed soil temperature and within 1 K for all the
307 sites and cases shown (Figure 7). However, the soil cools too quickly in the simulations. The temperature of the
308 surface is too warm overnight, by up to 4 K for the Skyborry site for IOP12, for all simulated cases with the exception
309 of IOP1. During IOP18 the MetUM is too warm at Cardington between 2100 UTC and 0400 UTC which is the period
310 of shallow stable radiation fog which is observed but not reproduced by the MetUM. The observed warming at 0300
311 UTC is caused by the optically thick fog which is not simulated until 0600 UTC (Figure 5). The behaviour described
312 here is, at least in part, a result of a soil heat flux which is significantly larger than observed by up to 50 W m^{-2} (Figure
313 8). Note here a positive soil heat flux is an upward flux towards the surface, so the MetUM is transferring heat to the
314 surface more readily than observed. This additional flux of heat is contributing to the surface temperature bias seen
315 for all cases and sites, with the exception of IOP1 at Cardington. The surface temperature bias will also contribute
316 to the near surface air temperature bias discussed in section 3.1, as the simulated screen temperature is calculated
317 using the surface temperature. Note the other components of the surface energy budget are modelled very closely
318 to those observed (not shown). In clear skies the net radiation flux is similar to the observed value but differences
319 occur due to cloud cover and fog optical thickness. IOP12 is a prime example of this with the large increase in surface
320 temperature at 0000 UTC caused by cloud which was observed but not simulated by the MetUM.

321 One possible reason for these differences could be biases in soil moisture leading to a bias in the soil thermal
322 conductivity. But an assessment of the soil moisture showed no systematic bias: some cases and sites were too moist

323 and others too dry, whereas all the cases had the soil heat flux bias. Previous studies have focussed on the impact
 324 of soil thermal conductivity on fog simulations in 1D models (Guedalia and Bergot, 1994; Bergot and Guedalia, 1994;
 325 Steeneveld and de Bode, 2018). These demonstrate a sensitivity to soil thermal conductivity either by perturbing a
 326 fixed value or by perturbing soil moisture. However, the JULES land surface model offers an alternative approach
 327 enabling an assessment to the sensitivity from uncertainties in the parametrisation of the relationship between soil
 328 thermal conductivity and soil moisture. Other parameters that may influence the soil heat flux are discussed in section
 329 4. The sensitivity to the soil thermal conductivity parametrisation is now examined.

330 JULES calculates the soil heat flux (G , $W m^{-2}$) via the following equation;

$$G = \nu[\sigma\epsilon\epsilon_s(T_*^4 - \sigma\epsilon\epsilon_s(T_{s1})^4) + \frac{\rho c_p}{r_{acan}}(T_* - T_{s1})] + (1 - \nu)\lambda_{soil}(T_* - T_{s1}) \quad (2)$$

331 where σ is the Stefan-Boltzmann constant, ϵ the emissivity of the vegetation, ϵ_s the emissivity of the soil, T_* the
 332 surface temperature, T_{s1} the soil level 1 temperature, ρ the air density, c_p the specific heat capacity of air, r_{acan} the
 333 aerodynamic resistance between the surface canopy of vegetation and the underlying soil and λ_{soil} the soil thermal
 334 conductivity (Best et al., 2011). Every JULES vegetation surface tile contains a fraction of bare soil and ν is the fraction
 335 of a tile that is vegetation with the remaining fraction bare soil. ν is a function of leaf area index and represents the
 336 direct interaction of the atmosphere with soil over an area of vegetation. JULES contains options for two methods
 337 of calculating the soil thermal conductivity (Best et al., 2011). The control simulations use the Dharssi et al. (2009)
 338 method which is a simplified version of Johansen (1975) which relates soil thermal conductivity and soil moisture:

$$\lambda = (\lambda_s - \lambda_{dry})K_e + \lambda_{dry} \quad (3)$$

339 where K_e is the Kersten number

$$K_e = \begin{cases} \log(\theta/\theta_s) + 1 & \text{if } (\theta/\theta_s) \geq 0.1 \\ 0 & \text{Otherwise} \end{cases} \quad (4)$$

340

$$\lambda_s = \frac{\lambda_{water}^{\theta_s} \lambda_{ice}^{\theta_f^s}}{\lambda_{water}^{\theta_s}} \lambda_s^u \quad (5)$$

341

$$\lambda_s^u = 1.58 + 12.4(\lambda_{dry} - 0.25) \quad (6)$$

342 and where λ is the thermal conductivity of soil, λ_s is the thermal conductivity of saturated soil, λ_{water} is the
 343 thermal conductivity of water, λ_{ice} is the thermal conductivity of ice, λ_{dry} is the thermal conductivity of dry soil, θ is
 344 soil moisture concentration, θ_s is soil moisture concentration at saturation, λ_s^u is the unfrozen saturated soil thermal
 345 conductivity which is constrained to $1.58 \leq \lambda_s^u \leq 2.2$. $\theta_f^s = \theta_s[S_f/(S_u + S_f)]$, $\theta_u^s = \theta_s - \theta_f^s$ where S_u and S_f are the
 346 unfrozen and frozen water contents as a fraction of saturation.

347 An alternative scheme, described in Cox et al. (1999), relates soil thermal conductivity and soil moisture as;

$$\lambda = (\lambda_s - \lambda_{dry})\theta/\theta_s + \lambda_{dry} \quad (7)$$

$$\lambda_s = \lambda_{water}^{\theta_s^w} \lambda_{ice}^{\theta_s^i} \lambda_{dry} / \lambda_{air}^{\theta_s} . \quad (8)$$

348 Best et al. (2011) state that the Cox et al. (1999) scheme generally gives smaller values of soil thermal conductivity,
 349 so it is expected to lead to smaller heat fluxes and lower surface temperatures. To assess the sensitivity of fog forecasts
 350 in the sub-km scale MetUM to the soil thermal conductivity parametrisation the UM333 was re-run for all cases with
 351 the Cox et al. (1999) scheme, these sensitivity simulations are referred to as C99 hereafter.

352 For C99 there is a reduction in the soil heat flux of up to 10 W m^{-2} in all cases and locations, although, the soil heat
 353 fluxes are still larger than observed ($30 - 60 \text{ W m}^{-2}$ compared to $10 - 30 \text{ W m}^{-2}$, figure 8). The reduction in the soil
 354 heat flux impacts the other components of the surface energy budget. Both the sensible and latent heat fluxes, when
 355 the boundary-layer is stable, are reduced by less than 1 W m^{-2} . The remaining energy reduction is in the upwelling
 356 longwave flux due to a decrease in surface temperature of approximately 2 K (Figure 7). The reduction in surface
 357 temperature is generally in better agreement with the observations (over all IOPs, 6 out of 7 times the C99 is in better
 358 agreement with the observations). IOP1 is the case when the surface temperature is not in better agreement with the
 359 observations; here there is an initial cold bias in the soil temperature of 1 K and thus the poorer surface temperature
 360 evolution in the C99 can in part be apportioned to the soil temperature bias.

361 In all scenarios the C99 simulations produce fog earlier (Figure 9). For example in IOP1 the C99 scheme results
 362 in fog formation 4 hours earlier than the control, closer to the observed onset time. The C99 also allows the UM333
 363 to produce fog at both sites during IOP17. For valley sites in IOP12 the C99 scheme is able to form fog, within
 364 two distinct periods, as observed - although the break in the fog is not at the correct time (which is related to the
 365 transient cloud layer). The hill site, Springhill, now produces fog for a longer duration which is in poor agreement
 366 with the observations, despite the Springhill surface temperature and ground heat flux coming closer to the observed
 367 values before the cloud layer advects over Springhill. However, the difference between the model and observations
 368 after midnight appears to be caused by differences in the cloud layer and how the model responds to this feature.
 369 Finally, despite the C99 producing surface temperatures closer to those observed between 2100 UTC and 0400 UTC
 370 at Cardington during IOP18, it is still unable to capture the shallow stable fog observed at this time.

371 In summary, the UM333 with the Cox et al. (1999) scheme produces fog earlier than with the Dharssi et al.
 372 (2009) scheme, which is generally in better agreement with the observations. Other model issues, for example the
 373 transient cloud layer, appear to be responsible for the periods where there is a degradation in the forecast arising from
 374 this change in the soil thermal conductivity scheme. Furthermore, the Cox et al. (1999) scheme produces surface
 375 temperatures and a lower soil heat flux in better agreement with the observations. In situations when the surface
 376 temperature is in worse agreement, the duration of the fog is still in better agreement with the observations.

377 4 | DISCUSSION

378 We have shown that biases in the soil heat flux lead to a degradation in the skill of simulations of fog in a sub-km
 379 scale NWP model. Using an alternative soil thermal conductivity parametrisation reduces the bias in the soil heat flux
 380 and typically improves the surface temperature and fog evolution. Previous studies have highlighted the sensitivity
 381 of fog simulations in a 1D context that do not include advection and any heterogeneity in soil properties (Bergot and
 382 Guedalia, 1994; Steeneveld and de Bode, 2018). We have shown for our four cases and various locations that the
 383 specification of the soil thermal conductivity can lead to a change in fog onset time of between 30 minutes and 5
 384 hours depending on the case. This is broadly in agreement with the up to 8 hour change in fog onset time found by
 385 Bergot and Guedalia (1994). We have demonstrated the critical importance of the soil parametrisations in recently

386 developed sub-km scale models as well as in the 1D context found in previous studies.

387 Other aspects of the model may also impact the soil heat flux. One aspect that impacts the soil thermal con-
388 ductivity and that can impact fog simulations is the soil moisture (Guedalia and Bergot, 1994; Maronga and Bosveld,
389 2017). We examined the MetUM soil moisture and found no systematic biases. A negative soil moisture bias, which
390 was seen in IOP17 and IOP18 and half the sites for IOP12, would result in a smaller soil thermal conductivity and
391 smaller soil heat flux. As the soil heat flux is systematically too large, the soil moisture errors were concluded not to be
392 the cause. Additionally, IOP1 with the Cox et al. (1999) scheme produced a surface temperature lower than observed
393 and it was the only case with an initial soil temperature bias indicating that in some cases the use of the Dharssi et al.
394 (2009) scheme could be compensating for errors in the initial soil temperature. This highlights the need for accurate
395 and representative soil measurements for data assimilation (Rémy and Bergot, 2009).

396 The LANFEX sites were all located over grass and as such all the model surface tiles are grass type. JULES
397 represents the thermal resistance of the grass canopy with the $\frac{\rho c_p}{r_{a,can}}(T_a - T_{s1})$ term of equation 2. Maronga and Bosveld
398 (2017) found that perturbing the soil moisture, in a large-eddy simulator, and consequently soil thermal conductivity
399 did not impact the fog onset time. However, they used a parametrisation that only accounted for the interaction of
400 the atmosphere with the surface canopy and no direct interaction with the soil. They stated this caused the lack of
401 sensitivity compared to previous studies that did not have canopy insulation and only modelled the interaction with
402 bare soil (Guedalia and Bergot, 1994). Every JULES vegetation surface tile contains a fraction of bare soil and ν is the
403 fraction of a tile that is vegetation with the remaining fraction bare soil. ν is a function of leaf area index (LAI) where
404 $\nu = 1 - e^{-K*LAI}$ and K is 1 (Bush et al., 2019). Even though the sites examined here are fully grass covered that does
405 not mean the grass fully insulates the surface from the soil in the manner of Maronga and Bosveld (2017). However,
406 the extent that a grass canopy insulates the soil from the atmosphere should be investigated further. Unlike previous
407 studies we have demonstrated the impact of soil thermal conductivity on simulations of fog using a surface scheme
408 which represents both canopy resistance and the direct interaction of the atmosphere with the soil. The model used
409 here allows for heterogeneities in the surface temperature over a few grid-lengths. The degree that surface property
410 heterogeneities impact fog simulations is not known and would be an interesting component of future research.

411 Whilst previous studies have shown that fog simulations are sensitive to the soil thermal conductivity either
412 by perturbing the soil thermal conductivity directly (Bergot and Guedalia, 1994; Steeneveld and de Bode, 2018) or
413 by perturbing the soil moisture (Guedalia and Bergot, 1994; Maronga and Bosveld, 2017) we have shown that the
414 simulations of fog are sensitive to the choice of parametrisation used to calculate soil thermal conductivity from soil
415 moisture emphasising the need to constrain these parametrisations better.

416 We have shown all our fog cases are impacted by biases in the soil heat flux. However, each case has its own
417 weaknesses that impact the fog simulation. A comparison of the three different grid-length simulations with the
418 radiosondes during IOP1 revealed a specific humidity bias of -1 g kg^{-1} in the lowest 1000 m of the atmosphere.
419 Adding an additional 1 g kg^{-1} within the lowest 1000 m resulted in the UM100 reproduced the fog depth closer to
420 the observed depth measured by the cloud droplet probe attached to the tethered balloon. Only IOP1 had a humidity
421 bias of this nature. The IOP1 humidity bias and sensitivity test highlights the need for accurate and representative
422 observations for data assimilation into fog forecasts.

423 The transient stratocumulus cloud layer during IOP12 was a challenge for the MetUM to reproduce, with the sub-
424 km configurations not producing any cloud between 0000 UTC and 0300 UTC and the UM1.5 simulation producing
425 too little. Fog simulations can be sensitive to the sub-grid cloud scheme (Tudor, 2010; Boutle et al., 2016). The sub-
426 grid cloud scheme represents the impact of sub-grid scale variability in humidity and thus partial cloudiness within
427 a grid box. Erroneous partial cloudiness caused by the sub-grid cloud scheme impacts the surface radiation budget,
428 consequently near-surface temperature and humidity and thus fog. The specification of RHCrit (recall RHCrit is the

429 grid-box mean relative humidity at which condensation begins to occur) has been shown to be case and grid-length
430 dependent (Boutle et al., 2016). Running the UM100 with the RHCrit value for the UM1.5 (see table 1) reproduced the
431 transient cloud layer closer to the observed cloud layer measured by the ceilometers at the main sites. This delayed
432 the fog formation from 0100 UTC at Skyborry (Figure 5) until 0400 UTC in better agreement with the onset time of
433 the second period of fog at 0300 UTC. The fog onset times at the other sites were almost unaffected by this change.
434 However, at the Springhill site the reduction to RHCrit resulted in a greater liquid water content value within the fog
435 layer despite no fog being observed. This case study is a prime example of the case and location dependent pitfalls
436 of current sub-grid cloud schemes. The development and implementation of schemes such as those of Furtado et al.
437 (2016) that removes the need to specify RHCrit but instead diagnoses the sub-grid scale humidity variability from
438 other model variables may be of use in the fog prediction and should be investigated. Ducongé et al. (2020) also
439 found this transient cloud layer to be a challenge to simulate using the Meso-NH model with a grid-length of 100 m
440 and found a sensitivity to the large scale forcing applied.

441 Identifying the cause of the case dependent issues for IOP17 and IOP18 is less clear cut. IOP17 highlights how
442 a sub-km scale model can capture very thin transient fog patches, that cannot be reproduced in lower resolution
443 configurations, as it reproduces additional variability in the near-surface temperature and humidity. The IOP18 fog
444 simulations are the least skilful of all the case with the UM100 performing the best producing fog at 0500 UTC instead
445 of at 2200 UTC as observed at Cardington. All IOP18 simulations contain a warm bias at screen level between 2200
446 UTC and 0400 UTC of approximately 1 - 2 K and a relative humidity bias of up to 8 %, independent of resolution
447 and soil thermal conductivity used. Thus other parametrisations for example turbulent mixing may be responsible for
448 performance.

449 5 | CONCLUSIONS

450 We have performed an assessment of three NWP model configurations, with three different grid-lengths; 1.5 km, 333
451 m and 100 m, of the MetUM for four selected LANFEX case studies. We present compelling evidence of the benefit
452 of using models at the sub-km scale for the numerical weather prediction of fog. The UM100 compared best to the
453 observations for wind and fog duration. At sites and for cases when the UM1.5 was unable to reproduce the observed
454 fog, the sub-km scale configurations are able to, with the UM100 closest to the observed duration of fog. However, a
455 warm bias within the valleys and a cold bias on the hills at night remains in the sub-km scale models. The temperature
456 bias is reduced compared to UM1.5, with the UM1.5 producing a bias of 2 K at 0000 UTC in the valleys and the
457 UM100 a bias of 0.5 K for the cases and sites in area of less complex orography. Similarly, in the more orographically
458 complex location the sub-km versions perform better in terms of the hill and valley temperature biases. The UM1.5
459 produced a valley warm bias of 1.5 K and a hill cold bias of 2 K whereas the UM333 produced a valley warm bias
460 of 1 K and a hill cold bias of 0.5 K. We have demonstrated the sub-km scale configurations offer an improvement
461 compare to the kilometre scale configuration producing the valley-hill temperature contrast better and consequently
462 producing the spatial variability in the fog life-cycle closer to observations. Previous work (e.g. Boutle et al., 2016
463 and Jayakumar et al., 2018) has focused on fog in cities where the urban surface heterogeneity has a large influence,
464 however, our findings show that there is also a benefit for more rural locations.

465 Biases in the surface temperature and soil heat flux were identified which were contributing to the valley warm
466 bias. Rerunning the UM333 with an alternative soil thermal conductivity parametrisation (Cox et al., 1999; C99)
467 reduced the soil heat flux bias and, in most cases, the improved surface temperature improved the timing of fog onset
468 suggesting this scheme should be tested further for km-scale and sub-km scale versions of the MetUM designed to

469 forecast fog, such as the London Model (Boutle et al., 2016) and the Delhi Model (Jayakumar et al., 2018). The Cox
470 et al. (1999) scheme appears to perform better than the Dharssi et al. (2009) scheme for foggy situations (although the
471 Cox et al. (1999) scheme still produces substantially higher soil heat fluxes compared to those observed). However,
472 this does not mean it would produce better forecasts in general. A more complex scheme such as the Johansen (1975)
473 scheme, which includes the impact of soil texture on soil thermal conductivity, could also offer improvements over
474 the simpler schemes currently available in JULES. Other models may also benefit from an investigation of their land
475 surface model given the sensitivity found here and the results of Steeneveld and de Bode (2018) who also found soil
476 thermal conductivity to be one of the most influential parameters on fog formation.

477 The experiments presented here illustrate how sensitive MetUM fog forecasts are to small changes in the land
478 surface model; fog formation up to 5 hours earlier arises from changing the method by which soil thermal conductivity
479 is calculated. To mitigate against this sensitivity a perturbed physics approach could be employed. For example,
480 McCabe et al. (2016) perturbed aspects of the microphysics and boundary-layer schemes for a MetUM simulated
481 fog event. They found this approach gave a greater ensemble spread and an improvement in the probabilistic skill
482 scores of visibility and temperature compared to a control ensemble. We suggest their approach could be extended
483 to include perturbations to the land surface model, for example the soil thermal conductivity. Recently Wang et al.
484 (2019) implemented perturbations to the land surface initial conditions and physics for a regional scale ensemble with
485 a resolution of 11 km which improved ensemble spread and reduced the mean ensemble bias for surface variables.
486 Here we have highlighted the key role the land surface model has on the numerical weather prediction of radiation fog
487 and we would emphasise that the development and evaluation of sub-km models is crucial for future improvements
488 of fog forecasts.

489 Acknowledgements

490 We would like to acknowledge our colleague the late Roland Von Glasow for securing the NERC Grant NE/M010325/1.
491 D. K. E. Smith was supported by NERC Grant NE/M010325/1. We acknowledge use of the Monsoon2 system, a col-
492 laborative facility supplied under the Joint Weather and Climate Research Programme, a strategic partnership between
493 the Met Office and the Natural Environment Research Council. The authors would like to thank everyone involved
494 in the collection and processing of the LANFEX data. The LANFEX data can be requested from the Met Office. The
495 MetUM was run using rose suite number u-ao450. The MetUM output is available by request from the first author.
496 We would also like to thank Peter Clark and Charles Chemel for discussions regarding this work which have improved
497 the final manuscript. We would like to thank the three anonymous reviewers for their constructive comments that
498 greatly improved the final manuscript.

499 References

- 500 Arakawa, A. and Lamb, V. R. (1977) Computational design of the basic dynamical processes of the UCLA general circulation
501 model. *General Circulation Models of the Atmosphere*, **17**, 173–265.
- 502 Baldocchi, D. and Waller, E. (2014) Winter fog is decreasing in the fruit growing region of the Central Valley of California.
503 *Geophysical Research Letters*, **41**, 3251–3256.
- 504 Bergot, T. and Guedalia, D. (1994) Numerical forecasting of radiation fog. Part I: Numerical model and sensitivity tests. *Monthly*
505 *Weather Review*, **122**, 1218–1230.
- 506 Bergot, T., Terradellas, E., Cuxart, J., Mira, A., Leichti, O., Mueller, M. and Nielsen, N. W. (2007) Intercomparison of single-
507 column numerical models for the prediction of radiation fog. *Journal of Applied Meteorology and Climatology*, **46**, 504–521.

- 508 Best, M. J., Pryor, M., Clark, D. B., Rooney, G. G., Essery, R. L. H., Ménard, C. B., Edwards, J. M., Hendry, M. A., Porson, A.,
509 Gedney, N., Mercado, L. M., Sitch, S., Blyth, E., Boucher, O., Cox, P. M., Grimmond, C. S. B. and Harding, R. J. (2011) The
510 Joint UK Land Environment Simulator (JULES), model description - Part 1: Energy and water fluxes. *Geoscientific Model*
511 *Development*, **4**, 677–699.
- 512 Boutle, I., Price, J., Kudszotsa, I., Kokkola, H. and Romakkaniemi, S. (2018) Aerosol–fog interaction and the transition to well-
513 mixed radiation fog. *Atmospheric Chemistry and Physics*, **18**, 7827–7840.
- 514 Boutle, I. A., Abel, S. J., Hill, P. G. and Morcrette, C. J. (2014a) Spatial variability of liquid cloud and rain: observations and
515 microphysical effects. *Quarterly Journal of the Royal Meteorological Society*, **140**, 583–594.
- 516 Boutle, I. A., Eyre, J. E. J. and Lock, A. P. (2014b) Seamless stratocumulus simulation across the turbulent gray zone. *Monthly*
517 *Weather Review*, **142**, 1655–1668.
- 518 Boutle, I. A., Finnenkoetter, A., Lock, A. and Wells, H. (2016) The London Model: forecasting fog at 333 m resolution. *Quarterly*
519 *Journal of the Royal Meteorological Society*, **142**, 360–371.
- 520 Bunce, R. G. H., Barr, C. J., Clarke, R. T., Howard, D. and Lane, A. M. J. (1990) ITE land classification of Great Britain 1990.
521 *NERC Environmental Information Data Centre*.
- 522 Bush, M., Allen, T., Bain, C., Boutle, I., Edwards, J., Finnenkoetter, A., Franklin, C., Hanley, K., Lean, H., Lock, A., Manners,
523 J., Mittermaier, M., Morcrette, C., North, R., Petch, J., Short, C., Vosper, S., Walters, D., Webster, S., Weeks, M., Wilkin-
524 son, J., Wood, N. and Zerroukat, M. (2019) The first Met Office Unified Model/JULES Regional Atmosphere and Land
525 configuration, RAL1. *Geoscientific Model Development Discussions*, **2019**, 1–47.
- 526 Chachere, C. N. and Pu, Z. (2019) Numerical simulations of an inversion fog event in the Salt Lake valley during the
527 MATERHORN-Fog field campaign. *Pure and Applied Geophysics*, **176**, 2139–2164.
- 528 Charney, J. G. and Phillips, N. A. (1953) Numerical integration of the quasi-geostrophic equations for barotropic and simple
529 baroclinic flows. *Journal of Meteorology*, **10**, 71–99.
- 530 Clark, P. A., Harcourt, S. A., Macpherson, B., Mathison, C. T., Cusack, S. and Naylor, M. (2008) Prediction of visibility and aerosol
531 within the operational Met Office Unified Model. I: Model formulation and variational assimilation. *Quarterly Journal of*
532 *the Royal Meteorological Society*, **134**, 1801–1816.
- 533 Cleaton, S. (2015) Fog causes major disruption to flights at UK airports. <http://www.bbc.co.uk/news/uk-34695577>. Accessed:
534 2015-11-23.
- 535 Cox, P. M., Betts, R. A., Bunton, C. B., Essery, R. L. H., Rowntree, P. R. and Smith, J. (1999) The impact of new land surface
536 physics on the GCM simulation of climate and climate sensitivity. *Climate Dynamics*, **15**, 183–203.
- 537 Dharssi, I., Vidale, P. L., Verhoef, A., Macpherson, B., Jones, C. and Best, M. (2009) New soil physical properties implemented
538 in the Unified Model at PS18. *Met Office Technical Report 528*.
- 539 Ducongé, L., Lac, C., Vié, B., Bergot, T. and Price, J. D. (2020) Fog in heterogeneous environments: the relative importance of
540 local and non-local processes on radiative-advective fog formation. *Quarterly Journal of the Royal Meteorological Society*,
541 **Early View**.
- 542 Duynkerke, P. G. (1999) Turbulence, radiation and fog in Dutch stable boundary layers. *Boundary-Layer Meteorology*, **90**, 447–
543 477.
- 544 Edwards, J. and Slingo, A. (1996) Studies with a flexible new radiation code. I: Choosing a configuration for a large-scale model.
545 *Quarterly Journal of the Royal Meteorological Society*, **122**, 689–719.
- 546 Forthun, G. M., Johnson, M. B., Schmitz, W. G., Blume, J. and Caldwell, R. J. (2006) Trends in fog frequency and duration in
547 the southeast United States. *Physical Geography*, **27**, 206–222.

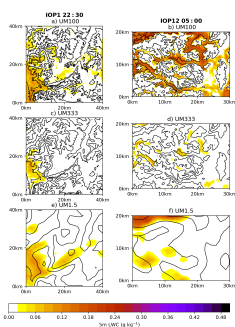
- 548 Furtado, K., Field, P. R., Boutle, I. A., Morcrette, C. J. and Wilkinson, J. M. (2016) A physically based subgrid parameterization
549 for the production and maintenance of mixed-phase clouds in a general circulation model. *Journal of the Atmospheric*
550 *Sciences*, **73**, 279–291.
- 551 Guedalia, D. and Bergot, T. (1994) Numerical forecasting of radiation fog. Part II: A comparison of model simulation with
552 several observed fog events. *Monthly Weather Review*, **122**, 1231–1246.
- 553 Gultepe, I., Fernando, H. J. S., Pardyjak, E. R., Hoch, S. W., Silver, Z., Creegan, E., Leo, L. S., Pu, Z., De Wekker, S. F. J. and Hang,
554 C. (2016) An overview of the MATERHORN fog project: Observations and predictability. *Pure and Applied Geophysics*,
555 **173**, 2983–3010.
- 556 Gultepe, I., Sharman, R., Williams, P. D., Zhou, B., Ellrod, G., Minnis, P. and Trier, S., Griffin, S., Yum, S. S., Gharabaghi, B. et al.
557 (2019) A review of high impact weather for aviation meteorology. *Pure and Applied Geophysics*, **176**, 1869–1921.
- 558 Gultepe, I., Tardif, R., Michaelides, S. C., Cermak, J., Bott, A., Bendix, J., Müller, M. D., Pagowski, M., Hansen, B., Ellrod, G.,
559 Jacobs, W., Toth, G. and Cober, S. G. (2007) Fog research: A review of past achievements and future perspectives. *Pure*
560 *and Applied Geophysics*, **164**, 1121–1159.
- 561 Hang, C., Nadeau, D. F., Gultepe, I., Hoch, S. W., Román-Cascón, C., Pryor, K., Fernando, H. J. S., Creegan, E. D., Leo, L. S.,
562 Silver, Z. and Pardyjak, E. R. (2016) A case study of the mechanisms modulating the evolution of valley fog. *Pure and*
563 *Applied Geophysics*, **173**, 3011–3030.
- 564 Hughes, J. K., Ross, A. N., Vosper, S. B., Lock, A. P. and Jemmett-Smith, B. C. (2015) Assessment of valley cold pools and clouds
565 in a very high resolution NWP model. *Geoscientific Model Development Discussions*, **8**, 4453–4486.
- 566 Jayakumar, A., Rajagopal, E. N., Boutle, I. A., George, J. P., Mohandas, S., Webster, S. and Aditi, S. (2018) An operational fog
567 prediction system for Delhi using the 330 m Unified Model. *Atmospheric Science Letters*, **19**, e796.
- 568 Johansen, O. (1975) *Thermal conductivity of soils*. Ph.D. thesis, University of Trondheim, Norway.
- 569 Kapoor, P. (2019) Over 10,000 lives lost in fog-related road crashes. Times of India [https://timesofindia.indiatimes.com/
570 india/over-10000-lives-lost-in-fog-related-road-crashes/articleshow/67391588.cms](https://timesofindia.indiatimes.com/india/over-10000-lives-lost-in-fog-related-road-crashes/articleshow/67391588.cms). Accessed: 2019-09-19.
- 571 Köhler, C., Steiner, A., Saint-Drenan, Y., Ernst, D., Bergmann-Dick, A., Zirkelbach, M., Bouallègue, Z. B., Metzinger, I. and Ritter,
572 B. (2017) Critical weather situations for renewable energies – Part B: Low stratus risk for solar power. *Renewable Energy*,
573 **101**, 794 – 803.
- 574 Lean, H. W., Barlow, J. F. and Halios, C. H. (2019) The impact of spin-up and resolution on the representation of a clear
575 convective boundary layer over London in order 100 m grid-length versions of the Met Office Unified Model. *Quarterly*
576 *Journal of the Royal Meteorological Society*, **145**, 1674–1689.
- 577 Li, C., Zelený, D., Chytrý, M., Chen, M., Chen, T., Chiou, C., Hsia, Y., Liu, H., Yang, S., Yeh, C. et al. (2015) Chamaecyparis
578 montane cloud forest in Taiwan: ecology and vegetation classification. *Ecological Research*, **30**, 771–791.
- 579 Lin, C., Zhang, Z., Pu, Z. and Wang, F. (2017) Numerical simulations of an advection fog event over Shanghai Pudong Interna-
580 tional Airport with the WRF model. *Journal of Meteorological Research*, **31**, 874–889.
- 581 Lock, A. P., Brown, A. R., Bush, M. R., Martin, G. M. and Smith, R. N. B. (2000) A new boundary layer mixing scheme. Part I:
582 Scheme description and single-column model tests. *Monthly Weather Review*, **128**, 3187–3199.
- 583 Maronga, B. and Bosveld, F. (2017) Key parameters for the life cycle of nocturnal radiation fog: a comprehensive large-eddy
584 simulation study. *Quarterly Journal of the Royal Meteorological Society*, **143**, 2463–2480.
- 585 McCabe, A., Swinbank, R., Tennant, W. and Lock, A. (2016) Representing model uncertainty in the Met Office convection-
586 permitting ensemble prediction system and its impact on fog forecasting. *Quarterly Journal of the Royal Meteorological*
587 *Society*, **142**, 2897–2910.

- 588 Müller, M. D., Masbou, M. and Bott, A. (2010) Three-dimensional fog forecasting in complex terrain. *Quarterly Journal of the*
589 *Royal Meteorological Society*, **136**, 2189–2202.
- 590 Nemery, B., Hoet, P. and Nemmar, A. (2001) The Meuse Valley fog 1930: An air pollution disaster. *The Lancet*, **357**, 704–708.
- 591 Poku, C., Ross, A. N., Blyth, A. M., Hill, A. A. and Price, J. D. (2019) How important are aerosol–fog interactions for the
592 successful modelling of nocturnal radiation fog? *Weather*, **74**, 237–243.
- 593 Porson, A., Price, J., Lock, A. and Clark, P. (2011) Radiation fog. Part II: Large-eddy simulations in very stable conditions.
594 *Boundary-Layer Meteorology*, **139**, 193–224.
- 595 Price, J., Porson, A. and Lock, A. (2015) An observational case study of persistent fog and comparison with an ensemble
596 forecast model. *Boundary-Layer Meteorology*, **155**, 301–327.
- 597 Price, J. D. (2011) Radiation fog. Part I: Observations of stability and drop size distributions. *Boundary-Layer Meteorology*, **139**,
598 167–191.
- 599 – (2019) On the formation and development of radiation fog: An observational study. *Boundary-Layer Meteorology*, **172**,
600 167–197.
- 601 Price, J. D., Lane, S., Boutle, I. A., Smith, D. K. E., Bergot, T., Lac, C., Duconge, L., McGregor, J., Kerr-Munslow, A., Pickering, M.
602 and Clark, R. (2018) LANFEX: A field and modeling study to improve our understanding and forecasting of radiation fog.
603 *Bulletin of the American Meteorological Society*, **99**, 2061–2077.
- 604 Pu, Z., Chachere, C. N., Hoch, S. W., Pardyjak, E. and Gultepe, I. (2016) Numerical prediction of cold season fog events over
605 complex terrain: the performance of the WRF model during MATERHORN-fog and early evaluation. *Pure and Applied*
606 *Geophysics*, **173**, 3165–3186.
- 607 Rémy, S. and Bergot, T. (2009) Assessing the impact of observations on a local numerical fog prediction system. *Quarterly*
608 *Journal of the Royal Meteorological Society*, **135**, 1248–1265.
- 609 Román-Cascón, C., Steeneveld, G. J., Yagüe, C., Sastre, M., Arrillaga, J. A. and Maqueda, G. (2016) Forecasting radiation fog at
610 climatologically contrasting sites: evaluation of statistical methods and WRF. *Quarterly Journal of the Royal Meteorological*
611 *Society*, **142**, 1048–1063.
- 612 Schemenauer, R. S., Fuenzalida, H. and Cereceda, P. (1988) A neglected water resource: The Camanchaca of South America.
613 *Bulletin of the American Meteorological Society*, **69**, 138–147.
- 614 Smith, D. K. E., Renfrew, I. A., Price, J. D. and Dorling, S. R. (2018) Numerical modelling of the evolution of the boundary layer
615 during a radiation fog event. *Weather*, **73**, 310–316.
- 616 Smith, R. N. B. (1990) A scheme for predicting layer clouds and their water content in a general circulation model. *Quarterly*
617 *Journal of the Royal Meteorological Society*, **116**, 435–460.
- 618 Steeneveld, G. and de Bode, M. (2018) Unravelling the relative roles of physical processes in modelling the life cycle of a warm
619 radiation fog. *Quarterly Journal of the Royal Meteorological Society*, **144**, 1539–1554.
- 620 Steeneveld, G. J., Ronda, R. J. and Holtslag, A. A. M. (2014) The challenge of forecasting the onset and development of
621 radiation fog using mesoscale atmospheric models. *Boundary-Layer Meteorology*, **154**, 265–289.
- 622 Tanaka, H., Honma, S., Nishi, M., Igarashi, T., Teramoto, S., Nishio, F. and Abe, S. (1998) Acid fog and hospital visits for asthma:
623 an epidemiological study. *European Respiratory Journal*, **11**, 1301–1306.
- 624 Tudor, M. (2010) Impact of horizontal diffusion, radiation and cloudiness parameterization schemes on fog forecasting in
625 valleys. *Meteorology and Atmospheric Physics*, **108**, 57–70.

- 626 Van der Velde, I. R., Steeneveld, G. J., Wichers Schreur, B. G. J. and Holtslag, A. A. M. (2010) Modeling and forecasting the
627 onset and duration of severe radiation fog under frost conditions. *Monthly Weather Review*, **138**, 4237–4253.
- 628 Von Glasow, R. and Bott, A. (1999) Interaction of radiation fog with tall vegetation. *Atmospheric Environment*, **33**, 1352–2310.
- 629 Vosper, S., Carter, E., Lean, H., Lock, A., Clark, P. and Webster, S. (2013) High resolution modelling of valley cold pools. *Atmo-
630 spheric Science Letters*, **14**, 193–199.
- 631 Vosper, S. B., Hughes, J. K., Lock, A. P., Sheridan, P. F., Ross, A. N., Jemmett-Smith, B. and Brown, A. R. (2014) Cold-pool
632 formation in a narrow valley. *Quarterly Journal of the Royal Meteorological Society*, **140**, 699–714.
- 633 Walters, D., Baran, A. J., Boutle, I., Brooks, M., Earnshaw, P., Edwards, J., Furtado, K., Hill, P., Lock, A., Manners, J., Morcrette,
634 C., Mulcahy, J., Sanchez, C., Smith, C., Stratton, R., Tennant, W., Tomassini, L., Van Weverberg, K., Vosper, S., Willett, M.,
635 Browse, J., Bushell, A., Carslaw, K., Dalvi, M., Essery, R., Gedney, N., Hardiman, S., Johnson, B., Johnson, C., Jones, A.,
636 Jones, C., Mann, G., Milton, S., Rumbold, H., Sellar, A., Ujiie, M., Whitall, M., Williams, K. and Zerroukat, M. (2019) The
637 Met Office Unified Model Global Atmosphere 7.0/7.1 and JULES Global Land 7.0 configurations. *Geoscientific Model
638 Development*, **12**, 1909–1963.
- 639 Walters, D., Boutle, I., Brooks, M., Melvin, T., Stratton, R., Vosper, S., Wells, H., Williams, K., Wood, N., Allen, T., Bushell, A.,
640 Copsey, D., Earnshaw, P., Edwards, J., Gross, M., Hardiman, S., Harris, C., Heming, J., Klingaman, N., Levine, R., Manners, J.,
641 Martin, G., Milton, S., Mittermaier, M., Morcrette, C., Riddick, T., Roberts, M., Sanchez, C., Selwood, P., Stirling, A., Smith,
642 C., Suri, D., Tennant, W., Vidale, P. L., Wilkinson, J., Willett, M., Woolnough, S. and Xavier, P. (2017) The Met Office Unified
643 Model Global Atmosphere 6.0/6.1 and JULES Global Land 6.0/6.1 configurations. *Geoscientific Model Development*, **10**,
644 1487–1520.
- 645 Wang, Y., Belluš, M., Weidle, F., Wittmann, C., Tang, J., Meier, F., Xia, F. and Keresturi, E. (2019) Impact of land surface
646 stochastic physics in ALADIN-LAEF. *Quarterly Journal of the Royal Meteorological Society*, **145**, 3333–3350.
- 647 Weston, M., Chaouch, N., Valappil, V., Temimi, M., Ek, M. and Zheng, W. (2019) Assessment of the sensitivity to the thermal
648 roughness length in Noah and Noah-MP land surface model using WRF in an arid region. *Pure and Applied Geophysics*,
649 **176**, 2121–2137.
- 650 Wilkinson, J. M., Porson, A. N. F., Bornemann, F. J., Weeks, M., Field, P. R. and Lock, A. P. (2013) Improved microphysical
651 parametrization of drizzle and fog for operational forecasting using the Met Office Unified Model. *Quarterly Journal of the
652 Royal Meteorological Society*, **139**, 488–500.
- 653 Wilson, D. R. and Ballard, S. P. (1999) A microphysically based precipitation scheme for the UK Meteorological Office Unified
654 Model. *Quarterly Journal of the Royal Meteorological Society*, **125**, 1607–1636.
- 655 Wood, N., Staniforth, A., White, A., Allen, T., Diamantakis, M., Gross, M., Melvin, T., Smith, C., Vosper, S., Zerroukat, M. and
656 Thuburn, J. (2014) An inherently mass-conserving semi-implicit semi-Lagrangian discretization of the deep-atmosphere
657 global non-hydrostatic equations. *Quarterly Journal of the Royal Meteorological Society*, **140**, 1505–1520.
- 658 Zhang, F. and Pu, Z. (2019) Sensitivity of Numerical Simulations of Near-Surface Atmospheric Conditions to Snow Depth and
659 Surface Albedo during an Ice Fog Event over Heber Valley. *Journal of Applied Meteorology and Climatology*, **58**, 797–811.

660 GRAPHICAL ABSTRACT

661 Fog remains a challenge to accurately forecast using numerical weather prediction. We
662 evaluate the performance of the Met Office Unified Model at both kilometre and sub-
663 kilometre **grid-lengths**. The MetUM produces valleys that are too warm and hills that are
664 too cold, leading to valleys that do not have enough fog and hills that have too much.
665 The sub-km scale configurations generally outperform the km scale but they are highly
666 sensitive to the soil thermal conductivity.



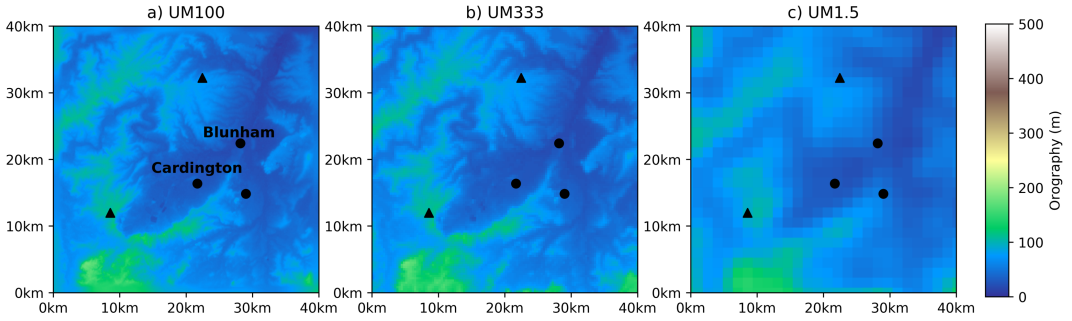


FIGURE 1 Model orography shown as height above mean sea level (m), for a) UM100, b) UM333 and c) UM1.5 in the UM100 Bedfordshire domain. Circles mark valley sites and triangles mark hill sites. Labelled sites are referred to in the text.

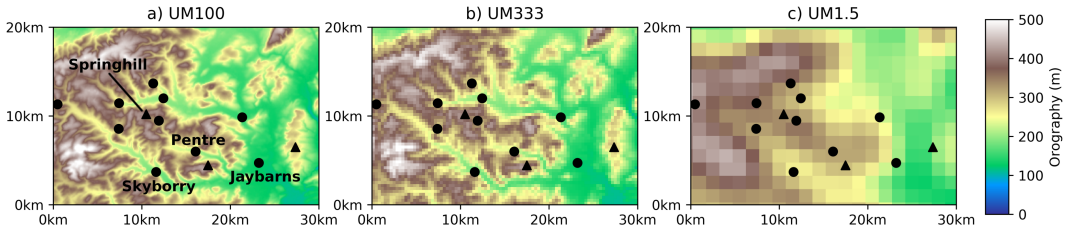


FIGURE 2 Model orography shown as height above mean sea level (m), for a) UM100, b) UM333 and c) UM1.5 in the centre of the UM100 Shropshire domain. Circles mark valley sites and triangles mark hill sites. Labelled sites are referred to in the text.

TABLE 1 Model configuration differences between simulations.

	UM100	UM333	UM1.5
Horizontal grid-length	100 m	333 m	1.5 km
Domain size Bedfordshire	40 km x 40 km	80 km x 80 km	1116 km x 1392 km
Domain size Shropshire	46 km x 35 km	80 km x 80 km	1116 km x 1392 km
Time step	4 s	12 s	60 s
RHCrit	0.99 at surface decreasing to 0.9 at 3.5 km, constant above	0.97 at surface decreasing to 0.9 at 3.5 km, constant above	0.96 at surface decreasing to 0.8 at 1 km, constant above
Number of vertical levels	140	70	70
Lowest model level	2 m	5 m	5 m

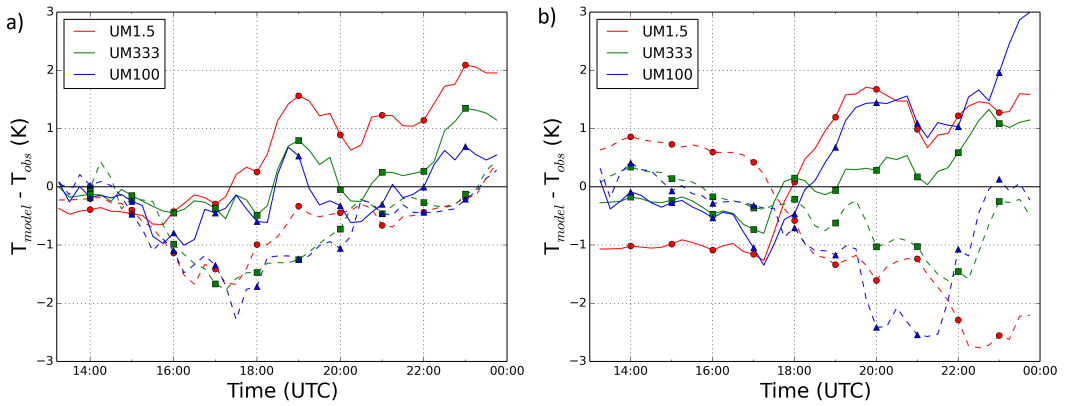


FIGURE 3 Temperature bias (K), 1.5 m model temperature - 1.5 m observed temperature, for the UM100 (blue), UM333 (green) and UM1.5 (red) simulations averaged for the valley (solid) and hill (dashed) sites for a) the average of all three Bedfordshire cases and b) the IOP12 Shropshire case.

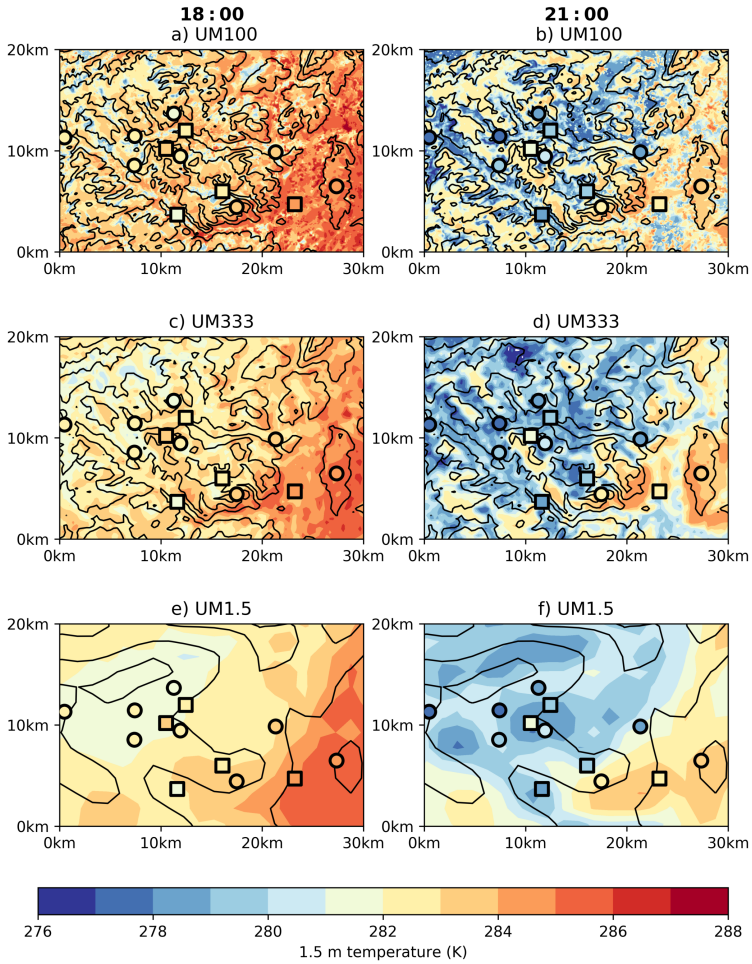


FIGURE 4 Screen-level temperature (K) for IOP12 at 1800 UTC (a,c,e) and 2100 UTC (b,d,f) for the UM100 (a,b), UM333 (c,d) and UM1.5 (e,f). Observations are overlaid as squares for the main sites and circles for the fog monitor sites. The black contours are orography in 100 m intervals.

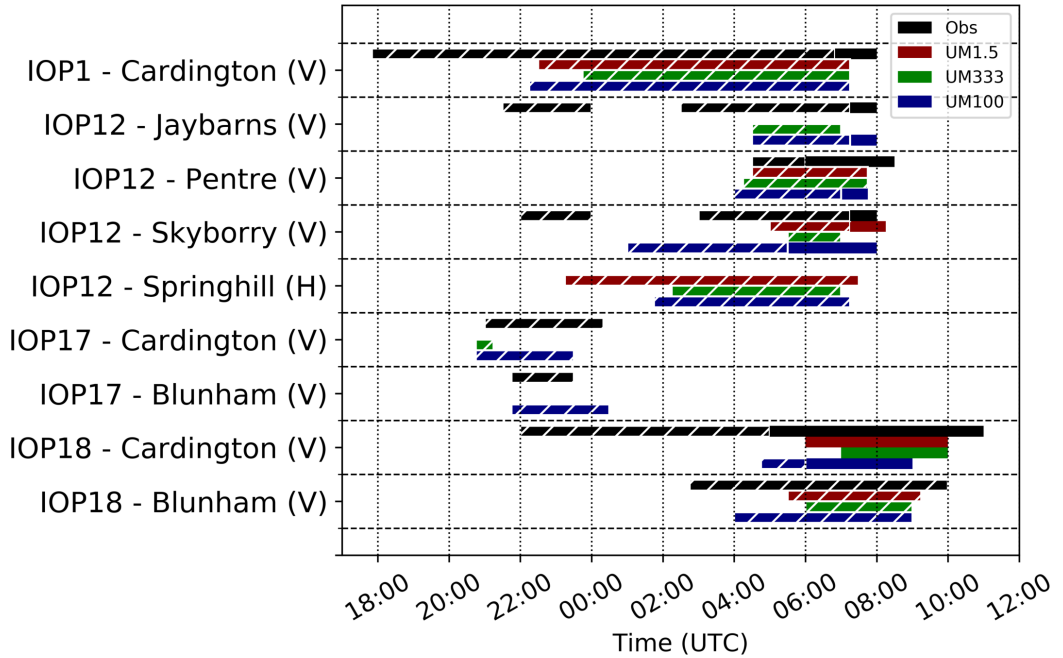


FIGURE 5 The duration of fog for all 4 case studies at selected sites for the observations (black), UM1.5 (red), UM333 (green) and UM100 (blue). Bars with hatching indicate shallow stable radiation fog and without hatching indicate deep adiabatic radiation fog. For the Blunham site boundary-layer stability cannot be assessed as only one temperature measurement is available. If no bar is plotted then no fog is present. The V indicates a valley site and H indicates a hill site.

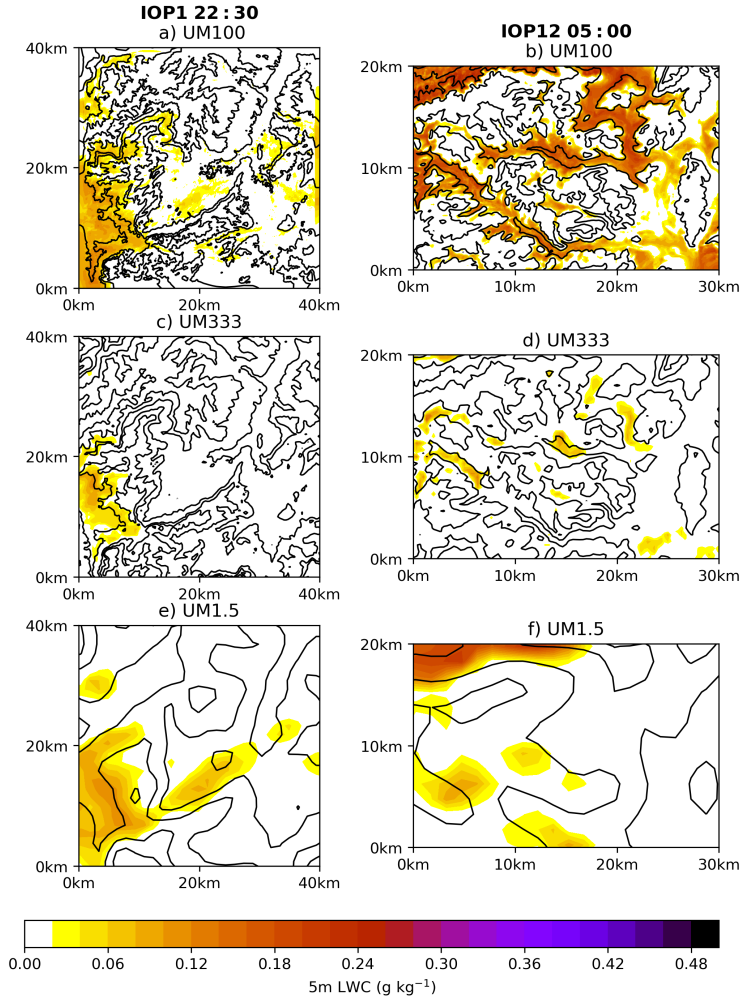


FIGURE 6 Liquid water content (g kg^{-1}) at 5 m for IOP1 at 22:30 (a,c,e) and IOP12 at 05:00 (b,d,f) for the UM100 (a,b), UM333 (c,d) and UM1.5 (e,f). The black contours are orography in 25 m intervals for a, c, e and 100 m intervals for b, d, f.

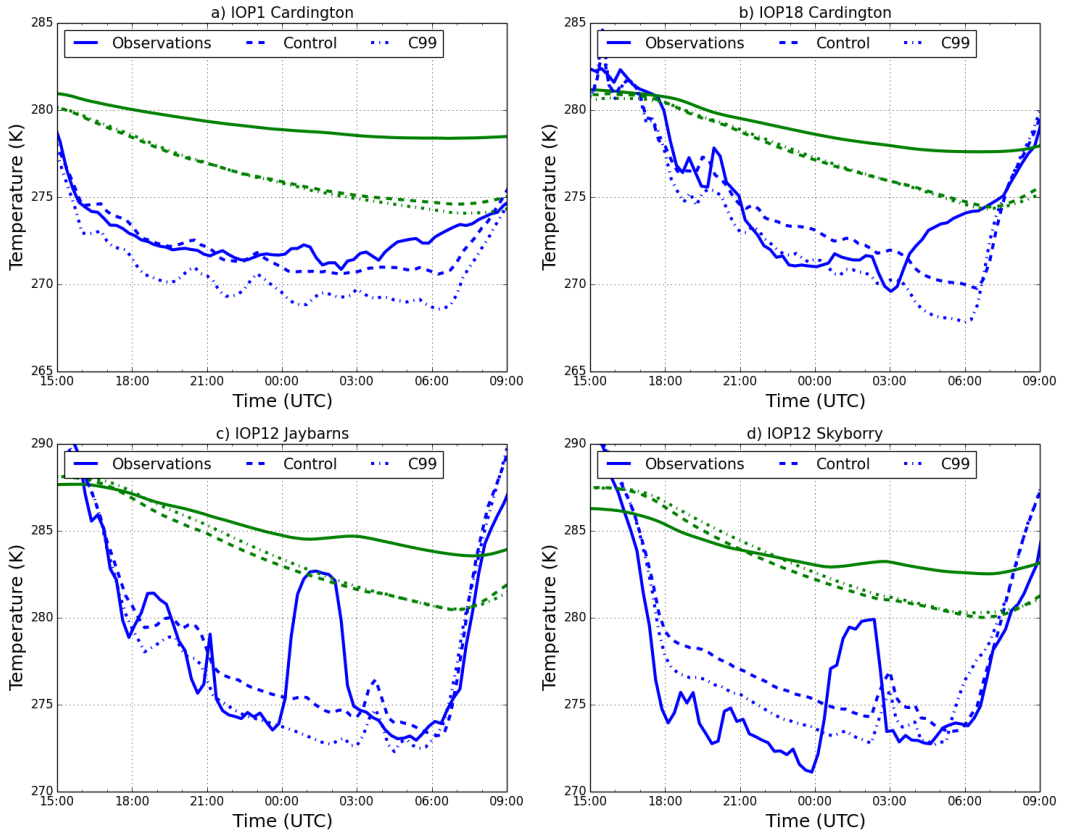


FIGURE 7 Soil temperature at 1 cm (K, Green) and surface temperature (K, Blue) for a) IOP1 Cardington, b) IOP18 Cardington, c) IOP12 Jaybarns and d) IOP12 Skyborry. Lines show observations (solid), control UM333 (dashed) and UM333 with the alternative soil thermal conductivity simulation based on Cox et al. (1999) (dot-dashed).

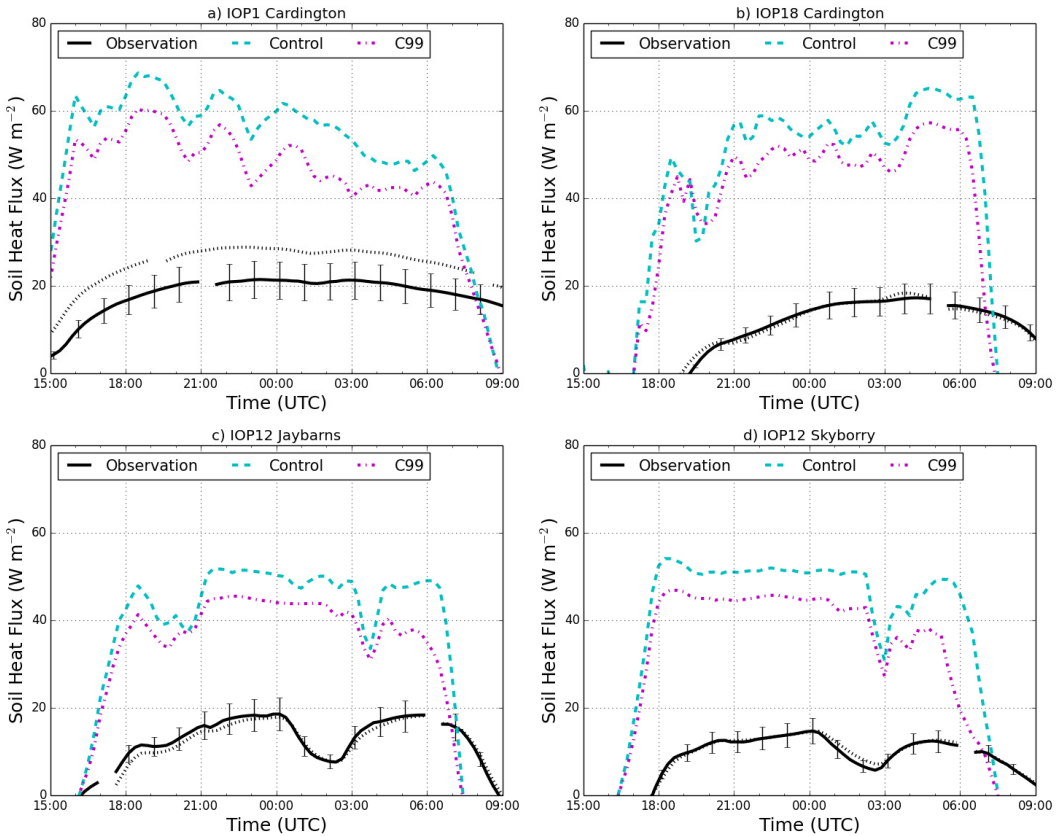


FIGURE 8 Observed (Black), control UM333 (Cyan) and UM333 with with the alternative soil thermal conductivity simulation based on Cox et al. (1999) (Magenta) soil heat fluxes (W m^{-2}) for a) IOP1 Cardington, b) IOP18 Cardington, c) IOP12 Jaybarns and d) IOP12 Skyborry. The dotted black line show the heat flux measured by an alternative Hukseflux HFP01SC-10 instrument. The error bars show the 20% uncertainty in the soil heat flux measurements.

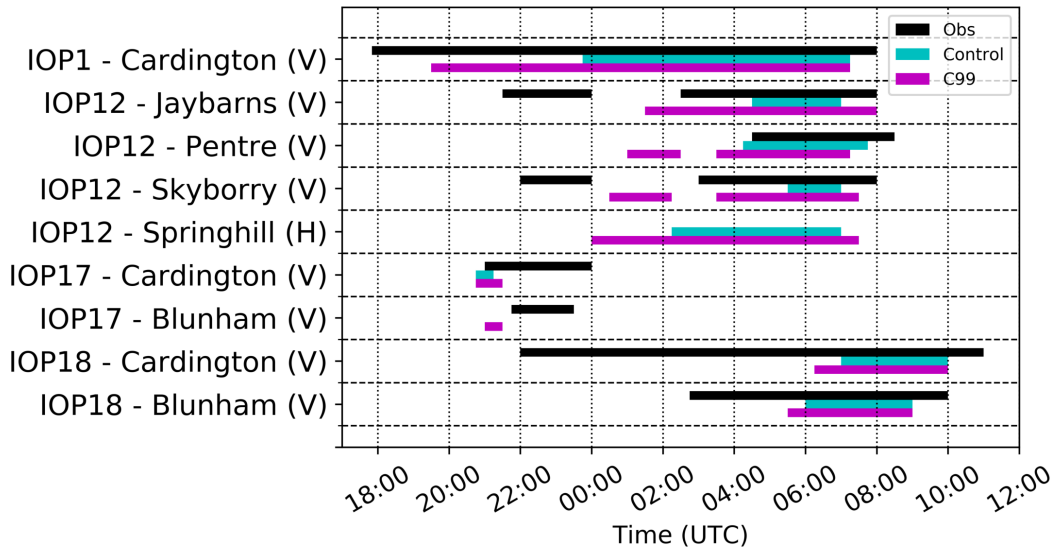


FIGURE 9 The duration of fog for all 4 selected case studies at selected sites for the observations (black), UM333 control (cyan) and UM333 with Cox et al. (1999) (magenta). The V marks valley sites and H marks hill sites.